THE JOURNAL OF PHYSICAL CHEMISTRY A

Article

pubs.acs.org/JPCA

Photoinitiated Dynamics in Amorphous Solid Water via Nanoimprint Lithography

Published as part of The Journal of Physical Chemistry virtual special issue "Veronica Vaida Festschrift".

Christopher Larson,[†] Yuanrui Li,[‡] Wei Wu,[‡] Hanna Reisler,*[,†] and Curt Wittig*[,†]

[†]Department of Chemistry and [‡]Department of Electrical Engineering, University of Southern California, Los Angeles, California 90089, United States

Supporting Information

ABSTRACT: Laser pulses that act on fragile samples often alter them irreversibly, motivating single-pulse data collection. Amorphous solid water (ASW) is a good example. In addition, neither well-defined paths for molecules to travel through ASW nor sufficiently small samples to enable molecular dynamics modeling have been achieved. Combining nanoimprint lithography and photoinitiation overcomes these obstacles. An array of gold nanoparticles absorbs pulsed (10 ns) 532 nm radiation and converts it to heat, and doped ASW films grown at about 100 K are ejected from atop the irradiated nanoparticles into vacuum. The nanoparticles are spaced from one another by sufficient distance that each acts independently. Thus, a temporal profile of ejected material is the sum of about 10^6 "nanoexperiments," yielding high single-pulse signal-to-noise ratios. The size of a single nanoparticle and its immediate surroundings is sufficiently small to enable modeling and simulation at the atomistic (molecular) level, which has not been feasible previously. An application to a chemical system is presented in which H/D scrambling is used to infer the presence of protons in films composed of D_2O and H_2O (each containing a small amount of HDO contaminant) upon which a small amount of NO_2 has been deposited. The pulsed laser heating of the nanoparticles promotes NO_2/N_2O_4 hydrolysis to nitric acid, whose protons enhance H/D scrambling dramatically.

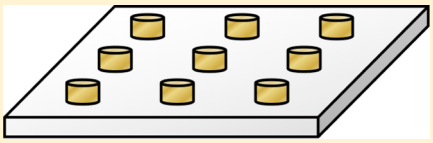

I. INTRODUCTION

Amorphous solid water (ASW) is ubiquitous throughout the Universe.[1−5] It plays a major role in the chemistry of the interstellar medium (ISM), where it coats dust particles in the giant molecular clouds that account for a quarter of the ISM mass and serve as a molecular factory.[6−9] These clouds are the birthplace of many of the polyatomic species that have been identified in the ISM.[10] Not surprisingly, the morphology of ASW is central to the accretion of molecules on (and dynamics on and in) the ASW-coated dust particles.[11]

In our own solar system each of the icy moons of Jupiter (Ganymede, Callisto, and Europa) and Saturn (Titan and Enceladus) harbors a submerged ocean under an uppermost layer of solid water. In all cases, the water (i.e., liquid plus solid) layer is much thicker than the average depth of Earth's oceans, which is 4 km. For example, Ganymede, the largest moon in our solar system, has a diameter of 5870 km (0.41 times Earth's diameter) and a thick layer of liquid and solid water. The overall amount of water is estimated to be at least several times that of Earth and possibly much more.[12] Europa and Enceladus have been identified as attractive candidates for primitive life forms near hydrothermal sources (vents) in their submerged oceans.[13,14] The possibility of a common origin of Earth's water and the water in the far reaches of our solar system and of primitive life forms has engendered great excitement,[15] and the recent discovery of H_2 being ejected from the subsurface ocean of Enceladus strongly supports this possibility.[14]

Enceladus has enjoyed center stage for more than a decade due mainly to the vast amount of data that has been gathered since 2004, when the spacecraft Cassini arrived at Saturn. Cassini has been orbiting Saturn since then, all the while transmitting data to Earth. Saturn's moon Enceladus is encased in 30−40 km of solid water that covers an 8−10 km thick submerged ocean. Tidal forces that involve Saturn and a 2:1 resonance with the moon Dione are responsible for water passing from its subsurface ocean into its sparse atmosphere.[16−19] Dramatic water jets have been observed that extend hundreds of kilometers above its southern polar region, though they account for a modest percentage of the material that issues from the fissures.[20−22] The water that enters the moon's atmosphere carries with it molecules. To date, 24 have been identified using mass spectrometry and deep ultraviolet (55−190 nm) absorption spectroscopy.[23,24]

Related laboratory experiments have focused on temperature-induced morphological changes in ASW and the accompanying release of water and embedded molecules. These experiments typically have used thin films deposited on low-temperature substrates under ultrahigh vacuum (UHV) conditions. Much has been learned: mechanisms of the explosive release of material (molecular volcanoes) initiated by increasing temperature through water's crystallization regime;[25−27] laser-initiated explosive release in doped and

Received: May 11, 2017
Published: June 5, 2017

DOI: 10.1021/acs.jpca.7b04560
J. Phys. Chem. A 2017, 121, 4968−4981

undoped ASW;[28] properties of highly viscous water and its glass transition;[29−31] eruptions initiated by pulsed laser heating of buried layers;[32] and more. Molecular-level modeling of thermal and laser-initiated dynamical processes has not been feasible, however, because of the unknown character of the fissures through which material passes on its way to vacuum, the large number of molecules that would need to be included, and the long time scales over which many observed phenomena take place.

In this article we introduce a strategy that complements, and in many cases provides advantages over, existing methods used in studies of thermally induced transport in ASW, including studies of photoinitiated thermal transport. It opens the door to a broad range of experiments and theoretical modeling of photoinitiated transport in doped and undoped ASW. In addition, complex chemical processes can be initiated and examined.

The idea is to use an array of gold nanoparticles that is heated using pulsed laser radiation. The particles are, reasonably speaking, identical to one another, and their shapes, dimensions, and intersite spacing can be controlled precisely and varied from one sample to the next. This control, in which the nanoparticles are heated using laser radiation that does not interact with the deposited films or substrates, is achieved by combining nanoimprint lithography and photoexcitation. This is the first report of this approach applied to the study of transport in ASW (H_2O and/or D_2O). It enables control over large arrays of heated nanoparticles without initiating processes in the regions between nanoparticles. The size of an individual nanoparticle and the interparticle spacing are such that molecular-level modeling and simulation can be applied to a single site. At the same time, millions of sites are accessed with a single 0.5 mm diameter laser pulse, ensuring a high single-shot signal-to-noise ratio (S/N).

Film deposition was performed near 100 K under UHV conditions, and 532 nm, 10 ns radiation heated the gold nanoparticle array. This caused molecules to enter vacuum, where they were detected using time-of-flight mass spectrometry (TOFMS) operating at 100 kHz, which enabled a complete mass spectrum to be obtained every 10 μs. The results differ significantly from those obtained earlier on transport and reactivity using layers of H_2O, D_2O, and N_2O_4 in sandwich configurations, with photoexcitation of the N_2O_4 layer.[32] The present results are in accord with the model introduced earlier, and they enable it to be refined. As mentioned above, it is of great importance that they open the door to molecular dynamics modeling and simulation.[33,34]

An application of the method to a complex chemical system is presented as a demonstration-of-principle. The hydrolysis of NO_2 at aqueous surfaces is known to yield nitrous and nitric acids HONO and HNO_3.[35−41] The weak acid HONO enters the gas phase, where its photolysis yields OH. HONO is a major source of OH in polluted environments, accounting for nearly all of the OH in the early hours of daylight and often 30−50% by afternoon. This, plus the fact that its presence in urban environments has many negative consequences, is well-documented.[35−41] How HONO is produced and gets into the atmosphere is not clear, however.

Finlayson-Pitts et al. proposed a model in which the asymmetric dimer, $ONONO_2$, converts in the presence of water to the nitrosonium nitrate ion pair NO^+ NO_3^-, which yields HONO and HNO_3.[42] Gerber and co-workers have examined this theoretically.[43−46] They predict that if the $ONONO_2$ configuration is reached in the presence of water, it evolves to NO^+ NO_3^- in just 20−30 fs,[43] and the ion pair yields HONO + HNO_3 in about a picosecond.[45] Pimentel and co-workers suggest an additional route,[47−49] though agreeing with most of the results of Gerber and co-workers. Other groups have contributed as well.[50,51] In all cases, the proposed mechanisms lack experimental verification of their viability, and major issues remain. For example, to what extent is the $ONONO_2$ configuration accessed under environmental conditions; what is the role of the lowest-energy isomer, which is symmetric N_2O_4; can experiments establish the presence of HONO and/or HNO_3 when the $ONONO_2$ configuration is accessed in the presence of water; can this be done on a short enough time scale to rule out other complex pathways?

The experimental results presented here confirm the presence of protons, which catalyze H/D scrambling, as H_2O and D_2O layers (plus a modest amount of HDO contaminant) mix and progress toward vacuum. Little scrambling takes place using alternate H_2O and D_2O layers alone, whereas a great deal of scrambling is observed with even modest NO_2 dosing. We conclude that nitric acid is produced. This is consistent with the proposed mechanism that starts with $ONONO_2$ and ends with HONO + HNO_3.[43−46] Whether $ONONO_2$ arises in polluted environments is altogether a separate issue.

The paper is organized as follows. In Section II experimental details specific to this work are presented. It is necessary to assess the extent of H/D scrambling that takes place on the chamber's exposed 300 K surfaces, as this sets the stage for the NO_2 experiments. Thus, Section III begins with a detailed description of experiments aimed at determining the fraction of HDO contaminant that is deposited on the cold array along with H_2O and D_2O. It then describes the photoinitiated heating of the gold nanoparticle array via plasmon resonance and transitions originating from gold d-orbitals. This is followed by results on HDO fractions observed upon first pulse irradiation, when the cold array is covered with layers of D_2O and H_2O, each containing a small fraction of HDO contaminant. Results on H/D scrambling when NO_2 is deposited atop the D_2O and H_2O layers are described in Section III.4, followed by an assessment that HNO_3 molecules desorbing from the 300 K walls are not the source of the observed proton-catalyzed H/D scrambling. Section III ends with a demonstration of the efficient heating enabled by the use of gold nanoparticles. Section IV summarizes the results and points to future directions of research.

II. EXPERIMENTAL DETAILS

Several important parts of the experimental arrangement are indicated schematically in Figure 1. Figures that show finer details and nuances are presented in Section III in the contexts of deposition and H/D scrambling. An electropolished ultrahigh vacuum (UHV) chamber (base pressure of several times 10^{-10} torr) is equipped with a high repetition rate (up to 200 kHz) TOFMS, a sample holder attached to a liquid N_2 cooling tube, and separate precision valves for introducing H_2O, D_2O, and NO_2. The TOFMS (Jordan TOF Products) was operated at 100 kHz in the experiments reported herein. The experiments were performed using pulsed (10 ns) 532 nm radiation (Nd:YAG laser second harmonic, Continuum PL9010, 10 Hz). Typically 0.4 mJ was focused to a 0.5 mm diameter spot at the film. A chopper wheel (ThorLabs MC1000, not shown) reduced the pulse rate at the surface to 1 Hz by selecting every 10th pulse. A telescope reduced the

DOI: 10.1021/acs.jpca.7b04560
J. Phys. Chem. A 2017, 121, 4968−4981

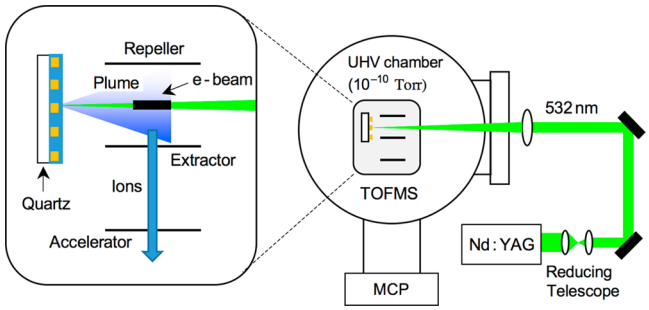

Figure 1. UHV chamber equipped with TOFMS: 532 nm radiation heats an array of gold nanoparticles coated with a film of ASW (100 K), causing material to enter the gas phase. The black rectangle labeled e-beam indicates the portion of the ionized region extracted through a circular mesh aperture in the extractor plate of the TOFMS. Ions are extracted at 100 kHz, that is, a complete mass spectrum is recorded every 10 μs.

beam diameter from 8 to 3 mm, and the beam was focused to a diameter of ≈0.5 mm at the surface using a 50 cm focal length CaF_2 lens.

A 10 × 10 × 1 mm^3 crystal quartz substrate (MTI Corporation) was patterned with an array of gold nanoparticles using nanoimprint lithography. A MgO substrate was also used, but it yielded results that did not differ in any significant way from those obtained using the crystal quartz substrate, so we report here results obtained using the crystal quartz substrate.

The separate precision leak valves for dosing H_2O, D_2O, and NO_2 are in different parts of the UHV chamber. Consequently, relative pressure readings recorded using a bare ionization gauge do not reflect directly the relative thicknesses of the deposited films. For example, calibration showed that equal pressure readings at the bare ionization gauge when H_2O and D_2O are introduced through their respective inlets correspond to deposition of 1.3 times more H_2O than D_2O. This will be discussed in Section III.1.a, where calibration data are presented. Deposition of NO_2 is more complicated, because there are both directed and background dosing contributions (see below and our previous publication).[32]

The gold nanoparticle array indicated in Figure 2 was prepared using nanoimprint lithography. First, a Si mother mold with a one-dimensional (1D) grating structure was fabricated using interference lithography. The grating line width

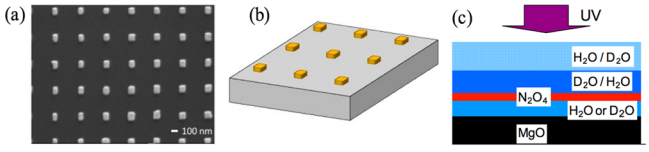

Figure 2. (a) SEM image of a lithographically prepared array of gold particles on silicon: 100 × 85 × 20 nm^3, rounded edges and corners, interparticle spacing of 400 nm. Silicon is used to illustrate the array, because it is suitable for SEM imaging, unlike the MgO and quartz insulators. Instrumental aberration causes particles to appear narrower going toward the left. (b) Illustrated dimensions, including height, of the gold nanoparticles excited using pulsed 532 nm radiation. (c) Illustrated sandwiches that were used in our earlier studies.[32] The lowest ASW layer insulates the N_2O_4 layer from the (high thermal conductivity) MgO substrate. The ASW above the N_2O_4 layer can be H_2O, D_2O, or a combination. The surface is maintained at ~100 K during deposition. Pulsed (10 ns) excitation at 355 or 266 nm acts on N_2O_4 without affecting the water or substrate.

was adjusted through thermal oxidation and HF etching. A polydimethylsiloxane (PDMS)-based flexible mold was duplicated from the mother mold and used to perform imprint and lift-off twice on a single Si substrate, resulting in a two-dimensional (2D) metal grid mask. After reactive ion etching, a 2D Si mold with a hole array was obtained, and another PDMS flexible mold with pillar array structure was duplicated from this Si mold. Finally, the 2D gold particle array was obtained by performing nanoimprint and liftoff using the PDMS flexible mold fabricated in the previous step. A gold nanoparticle array on a Si substrate was fabricated following the same procedure as with the reference sample. It was characterized using a scanning electron microscope (SEM; Figure 2a). Interparticle spacing is 400 nm, and each particle is 100 × 85 × 20 nm^3 with rounded edges and corners.

The gold-patterned quartz substrate was clamped in 0.3 mm thick copper foil (ESPI Metals) with a 6 × 6 mm^2 aperture to allow radiation to pass. The foil-clamped substrate was then mounted on one of two electrically isolated copper blocks connected to a liquid nitrogen filled cooling tube (Kurt Lesker; modified by McAllister Technical Services) capable of lowering the surface temperature to ≈90 K. The surface temperature was monitored using a K-type thermocouple cemented (Aremco Ceramabond 835-M) to the front of the substrate near the edge. The substrate could be resistively heated with a tantalum wire bonded to the backside of the substrate's foil housing. The liquid nitrogen cooling tube was mounted on a translation stage (VG Scienta). It was capable of XYZ translation and 360° rotation.

Samples were deposited immediately after heating the surface to 200 K to remove condensed background gas and then recooling. In the experiments reported here, the temperature was either near 100 K or near 110 K. These temperatures will be specified when appropriate; otherwise they will be referred to as ~100 K.

All gases except NO_2 were deposited using background dosing. Because of the reactivity of NO_2 with metal surfaces, it entered the chamber through a 0.75 cm ID × 23 cm glass tube fed by a precision leak valve. Thus, there are both directed dosing and background dosing components, as discussed previously.[32] The surface was 4 cm from the end of the glass tube during dosing. The H_2O, D_2O, and NO_2 samples were degassed using 2−3 freeze−pump−thaw cycles prior to their use. Each was kept in a separate line connected to its own precision leak valve to avoid contamination. The D_2O line was passivated for 1−2 h prior to experiments to minimize HDO contaminant when D_2O was admitted to the chamber. The vast majority of the HDO present in the deposited water arises from H/D scrambling on 300 K surfaces, as discussed in Section III.

The TOFMS is a Wiley−McLaren design with three electrode plates and an electron beam ionization source, whose center is 2.5 cm above the array, with a range of ±0.5 cm, as indicated in Figure 1. Extraction at 100 kHz yields a mass spectrum every 10 μs. Laser irradiation heats the gold nanoparticles through their efficient 532 nm absorption due to plasmon resonance and transitions originating from d-orbitals. This results in the ejection of deposited material into vacuum, with a plume of molecules passing through the (70 eV electron impact) ionization region. Repeller and extractor plates were held at 1800 V, and positive ions were extracted every 10 μs by dropping the potential on the extractor plate to 1550 V for 3 μs. Ions were then accelerated further using a grounded third plate, after which they entered the 48 cm field-free drift tube. They

DOI: 10.1021/acs.jpca.7b04560
J. Phys. Chem. A 2017, 121, 4968−4981

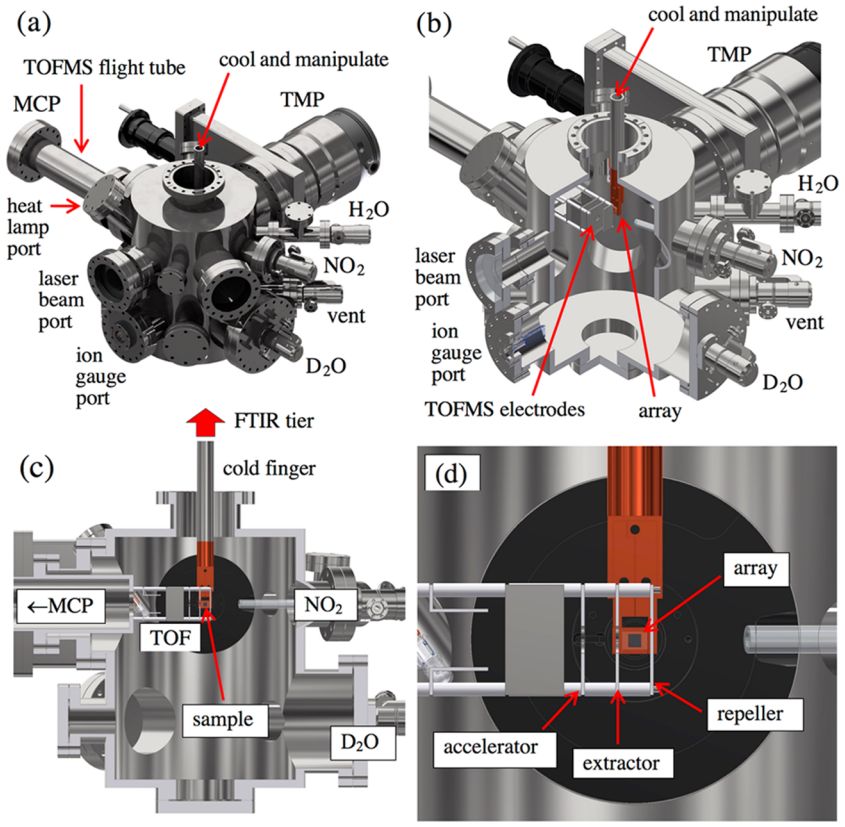

Figure 3. Schematic drawings of the main vacuum chamber. (a) Exterior view showing the turbomolecular pump (TMP), dosing leak valves, bare ionization gauge, heat lamp, window for laser beam, vent, TOFMS flight tube, and microchannel plates (MCP). (b) A three-quarter cut reveals the interior components. (c) A side view of the chamber, cut through the center plane of the TOFMS flight tube, shows the upper dosing inlets (H_2O and NO_2) and the lower dosing inlet (D_2O). (d) Expanded view, from panel (c), of the TOFMS electrodes and sample holder: The laser beam is incident to the surface in the direction perpendicular to the page. A gate valve above the top flange (not shown) is followed by the FTIR tier used in previous measurements.[32] The cold array was rotated by ≈100° during NO_2 dosing.

were further accelerated and detected at the end of the field-free region using a microchannel plate (MCP) detector connected to a fast preamplifier (SRS D-300 MHz). The amplified current from the MCP was recorded on a computer with an analogue-to-digital converter (Gage CS 8500, 8 bit, 512k samples). Spectra were collected using a custom LabView program (National Instruments) and further processed using IGOR Pro (WaveMetrics). The set of individual mass spectra collected following a single laser pulse is referred to as a temporal profile or simply a profile.

Because of defects in the quartz surface, eight spots in a 2 × 4 grid were chosen for irradiation for each deposited film. The eight temporal profiles were summed, thereby improving S/N and reducing effects due to laser energy fluctuation and film irregularity. Translating the array by 1 mm while keeping the laser beam fixed ensured irradiation of an undisturbed section of the film. The gold nanoparticles were found to be stable in the sense that there was no degradation of signal intensity over the course of this study. Atomic force microscopy scans after several months of experiments confirmed that the surfaces have good areas and bad areas and that the nanoparticles remained intact.

The 532 nm radiation does not interact with H_2O, D_2O, N_2O_4, and crystal quartz. However, free NO_2 has a 532 nm absorption cross section of 1×10^{-19} cm^2 at 298 K.[52,53] Typical laser fluence is ~0.2 J cm^{-2}, and the product $\sigma\Phi$, where σ is the absorption cross section and Φ is photons cm^{-2}, is ~0.05. On this basis, we conclude that ~5% of isolated NO_2 molecules absorb a photon and become vibrationally excited. This is not important at large NO_2 dosage, because nearly all the NO_2 is present as N_2O_4, which is transparent at 532 nm. It might play a role at small NO_2 dosage.

III. RESULTS AND DISCUSSION

III.1. D_2O and H_2O Deposition and H/D Scrambling.

The ASW films used in the present study were composed of two layers, namely, D_2O on the bottom and H_2O on the top. Our previous results using layered H_2O and D_2O systems showed no substantial difference when changing the order of the depositions,[32] so here we focus on the system of D_2O on the bottom and H_2O on top. The films were prepared by depositing water vapor onto the gold nanoparticle array bound to its crystal quartz substrate (together referred to hereafter as "the array") at a temperature of either 100 or 110 K, depending on the experiment. Because of the insidious problem of isotope exchange (H/D scrambling) on 300 K surfaces, determining the amounts of H_2O, D_2O, and HDO deposited on the cold array, including how their respective fractions vary throughout a given film, required attention to detail.

Referring to Figure 3, the flow rates of H_2O and D_2O into the chamber were controlled using precision leak valves, and pressure readings were recorded using the bare ionization gauge. When the chamber and its contents were exposed to a large amount of D_2O, say for a few hours prior to the introduction of H_2O, the exposed 300 K surfaces acquired

DOI: 10.1021/acs.jpca.7b04560
J. Phys. Chem. A 2017, 121, 4968−4981

significant amounts of deuterium, presumably in a range of chemisorbed and physisorbed species and states. When H_2O was then introduced, H/D scrambling took place on the exposed 300 K surfaces, as described in Section III.1.b. Recall that molecules entering the gas phase travel unimpeded from surface to surface at the low pressures used in the experiments, as there are practically no gas-phase collisions within the chamber.

The inevitable H/D scrambling on 300 K surfaces manifests as the deposition of HDO onto the cold array. When H_2O is admitted to the chamber after exposure to D_2O, the ion gauge pressure reading is of H_2O + HDO, and both H_2O and HDO are deposited onto the cold array. Likewise, when D_2O is then admitted to the chamber, the pressure reading is that of D_2O + HDO, and both D_2O and HDO are deposited onto the cold array. There is no reason to expect spatial homogeneity of gas-phase molecules and isotopologue fractions, and consequently the isotopologue fractions vary throughout the chamber in ways that are not obvious a priori. We shall address this subtle issue in Section III.1.b and show that it is central to interpretation of the experimental results.

There is an important difference in admitting H_2O versus D_2O into the chamber. Namely, their inlets are in different parts of the chamber, in which case these gases and their HDO progenies travel throughout the chamber in different ways before being pumped away or deposited on (1) the cold array, (2) the cold copper surfaces near the array, and (3) the 77 K cooling tube that extends upward through the topmost flange of the main chamber (Figure 3). Thus, there is no reason to believe that the deposition rates of H_2O + HDO (i.e., when H_2O is admitted to the chamber) and D_2O + HDO (i.e., when D_2O is admitted to the chamber) are equal when their ion gauge pressure readings are equal. It is also important that the cold array is near a cold Cu rod and the cooling tube, and the opening to the upper region that leads to the FTIR tier has the cooling tube near its center. The upper region plus the 77 K cooling tube serve as a cryopump that removes gas-phase water molecules more rapidly than the turbomolecular pump. This is described in detail in Appendix 1.

HDO fractions recorded by the TOFMS 2.5 cm above the cold array when H_2O and D_2O are admitted sequentially to the chamber are denoted, respectively, [HDO]/[H_2O + HDO] and [HDO]/[D_2O + HDO]. We assume that these fractions are preserved in the deposited material. This is equivalent to assuming that the isotopologue fractions of molecules that stick to the cold array come from 300 K surfaces that, on average, send equal fractions to the TOFMS ionization region and the cold array during deposition. In the following subsection, HDO fractions are determined as a function of exposure time, and on the basis of the assumed equivalence between the gas phase and deposited fractions, they indicate how HDO is distributed throughout films comprising layers of (mainly) D_2O and H_2O, each with embedded HDO. These data serve as the background against which the proton-catalyzed H/D scrambling discussed in Section III.4 is judged.

In previous work, we established the relationship between Langmuirs (L) of H_2O (using the bare ionization gauge) and how much water is deposited at 100 K; specifically, 1 L corresponds to 1.7 monolayers (ML).[54] This will be applied to the deposition of H_2O + HDO for a given pressure reading. The same applies to D_2O + HDO, albeit with an additional scale factor (discussed below) that accounts for the fact that the D_2O + HDO deposition rate differs from the H_2O + HDO deposition rate at the same pressure reading due to the different H_2O and D_2O inlet locations.

III.1.a. Calibration Data. As mentioned earlier, mass spectra recorded 2.5 cm above the cold array yielded HDO *fractions* when D_2O and H_2O were admitted to the chamber sequentially. These measurements also yielded TOFMS signals that are proportional to the *amount* of gas-phase water above the array: D_2O + HDO and H_2O + HDO when D_2O and H_2O, respectively, were admitted to the chamber sequentially. Examples of time-of-flight spectra are shown in Figure 4.

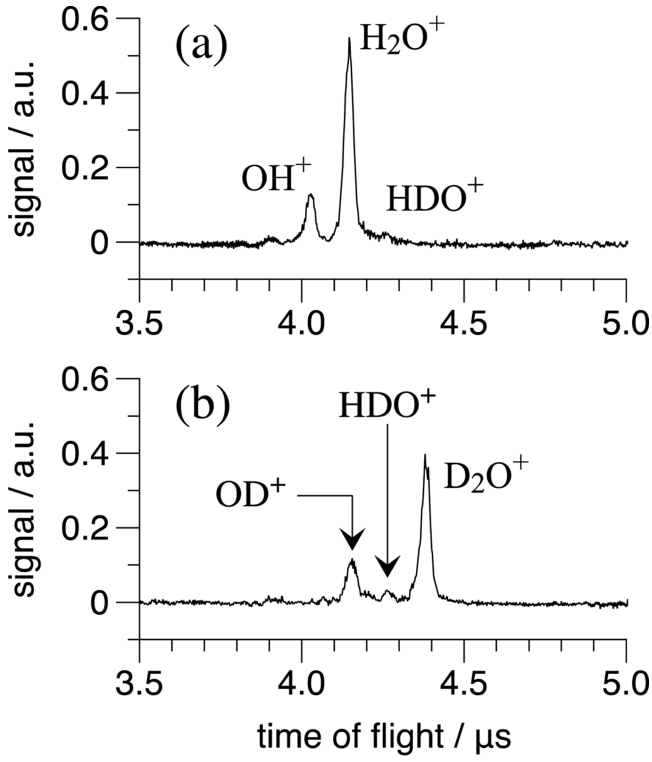

Figure 4. Representative time-of-flight traces for (a) H_2O + HDO and (b) D_2O + HDO, each recorded at a pressure reading of 2×10^{-7} torr, with the array at 110 K. The vertical scale (arbitrary units) is the same for (a) and (b). The total area of the peaks in (a) is proportional to the amount of gas-phase water present above the array; likewise, for trace (b). The ratio of these areas is 1.33. The ratio used in the text is 1.30. It is the median ratio from 45 spectra of each.

Comparison of the integrated signal strengths for 45 such spectra indicates 1.3 times more H_2O + HDO than D_2O + HDO above the cold array. This is a geometrical effect due to the different inlet locations. Even when the pressure gauge readings are the same when admitting H_2O and D_2O separately into the chamber, the amount of water deposited on the array is different. This is taken into account in data analyses.

III.1.b. H/D Scrambling on 300 K Surfaces. The H/D scrambling that takes place on 300 K surfaces involves complex processes in which H_2O and D_2O molecules adsorb and find available active surface sites that promote the formation of HDO, which subsequently enters the gas phase. Therefore, the extent of H/D scrambling depends on dosing sequence, as illustrated in Figure 5.

The stainless steel line carrying D_2O vapor to the precision leak valve was passivated for several hours before each experiment. In panel (a), a mass spectrum was recorded just after the D_2O flow was turned on, and the pressure reading was

DOI: 10.1021/acs.jpca.7b04560
J. Phys. Chem. A 2017, 121, 4968−4981

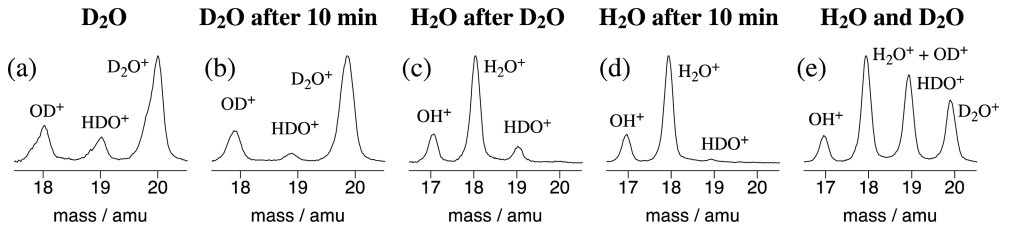

Figure 5. Mass spectra recorded with the chamber and array at 300 K. In (a)−(d), the pressure readings were 1×10^{-6} torr. In (e), D_2O and H_2O were present simultaneously, each at a partial pressure reading of 1×10^{-6} torr. Note the efficient scrambling in (e).

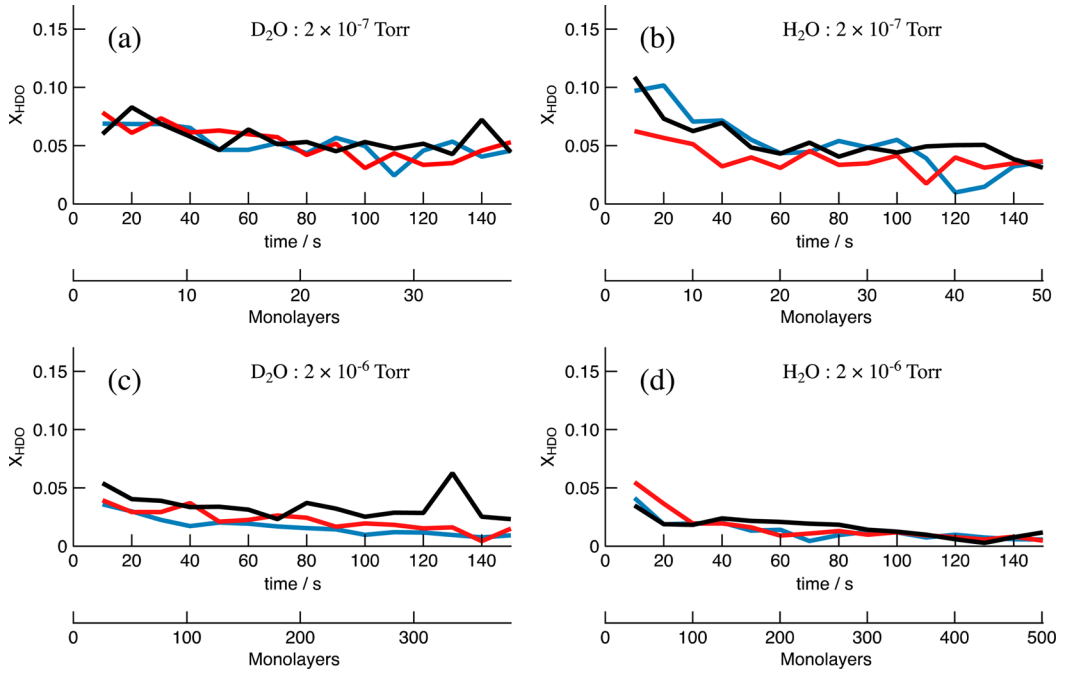

Figure 6. HDO fraction X_{HDO} vs exposure time in seconds when admitting $D_2O(H_2O)$ into the chamber with a cold array at a fixed pressure reading, followed by $H_2O(D_2O)$ at the same pressure reading. Mass spectra were recorded 2.5 cm above the 110 K array, and the X_{HDO} fractions were determined from peak areas (see text). (a) D_2O was admitted to the chamber for 150 s at a pressure reading of 2×10^{-7} torr. Spectra were recorded every 10 s, averaging 25 traces each time. (b) The fractions when H_2O is admitted to the chamber about a minute after turning off the D_2O. Note that deposition in Monolayers differs for (a) and (b). (c, d) Pressure reading of 2×10^{-6} torr. The black, red, and blue curves depict different sets of experiments, as described in the text.

maintained at 1×10^{-6} torr. Panel (b) shows a mass spectrum recorded after 10 min of admitting D_2O to the chamber at constant pressure. There is much less HDO due to the removal of hydrogen from active sites. The D_2O was then turned off, and the chamber was evacuated, reaching $\sim 1 \times 10^{-8}$ torr in a few seconds and $\sim 1 \times 10^{-9}$ torr in less than a minute. H_2O was then admitted at a pressure reading of 1×10^{-6} torr. Panel (c) shows a spectrum recorded immediately after H_2O is introduced, and panel (d) shows a spectrum taken after 10 min of H_2O exposure. Both panels (b) and (d) show a decrease in HDO signal as a function of increasing exposure time. In panel (e), the partial pressure readings were 1×10^{-6} torr each for D_2O and H_2O, which were admitted to the chamber simultaneously. Efficient scrambling was recorded. In all cases, 300 mass spectra were summed.

III.1.c. H/D Scrambling during Deposition. Deposition was achieved by introducing D_2O followed by H_2O. The gas-phase molecules present in the chamber during deposition are either D_2O and HDO, or H_2O and HDO, depending on whether D_2O or H_2O is being introduced. Mass spectra were recorded above the 110 K array at 10 s intervals for times appropriate to the deposition cycles. The TOFMS was operated at 100 kHz (10 μs per spectrum), and 25 TOF spectra were averaged every 10 s.

It is important to bear in mind that during deposition the extent of H/D scrambling on the 300 K surfaces depends on the dosing procedure for H_2O and D_2O and on chamber preparation: time spent under UHV, heating to remove adsorbed water, seasoning with D_2O or H_2O, etc. These factors are implicit in the term "exposure history." Figure 6 displays trends in H/D scrambling for cases in which D_2O and H_2O were admitted to the chamber sequentially, each for 150 s at the same pressure reading. The results are presented as the fractions $X_{HDO} = A_{19}/(A_{19} + A_{20})$ or $A_{19}/(A_{19} + A_{18})$, where A_{18}, A_{19}, and A_{20} are proportional to the peak areas of the time-of-flight traces corresponding to 18, 19, and 20 amu (see Appendix 2). The fraction $A_{19}/(A_{19} + A_{20})$ is used when D_2O is admitted to the chamber, and therefore $A_{18} = 0$; likewise, for H_2O $A_{19}/(A_{19} + A_{18})$ is used and $A_{20} = 0$. The delay between the end of the D_2O deposition and the start of the H_2O deposition in these experiments was about 1 min. The fractions presented in Figure 6a,b were obtained under conditions that are comparable to those used in the proton-catalyzed scrambling experiments discussed in Section III.4, specifically,

DOI: 10.1021/acs.jpca.7b04560
J. Phys. Chem. A 2017, 121, 4968−4981

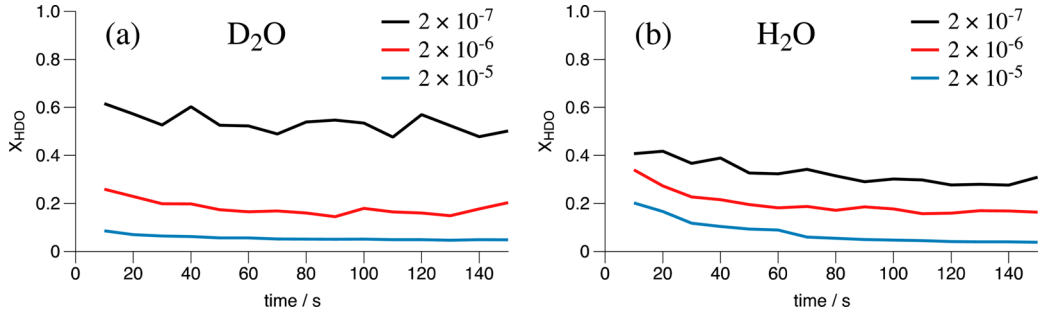

Figure 7. HDO fraction X_{HDO} vs exposure time in seconds when admitting $D_2O(H_2O)$ into the chamber at a fixed pressure reading, followed by $H_2O(D_2O)$ at the same pressure reading, with all surfaces at 300 K. Ion gauge readings were (in torr) 2×10^{-7} (black), 2×10^{-6} (red), and 2×10^{-5} (blue). (a) The chamber had been evacuated overnight to a few times 10^{-10} torr, and D_2O was admitted. (b) H_2O was admitted through its inlet starting about 1 min after turning off the D_2O, at which time the pressure reading was $\sim 1 \times 10^{-9}$ torr. H/D scrambling decreases with increasing pressure.

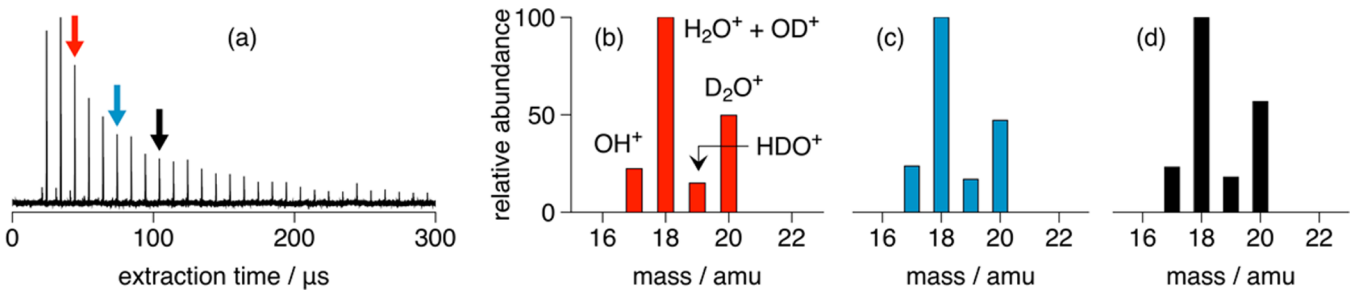

Figure 8. Deposition was performed at 100 K. D_2O was admitted to the chamber for 150 s at a pressure reading of 2×10^{-7} torr, yielding 39 ML. This was followed by admitting H_2O for 150 s at a pressure reading of 2×10^{-7} torr, yielding 50 ML. Pulsed irradiation (532 nm, 10 ns, 0.4 mJ, 0.5 mm diameter at the film) yielded the profile in (a), in which first-pulse profiles from eight spots were summed. The profiles consist of successive TOF spectra, each of 10 μs duration. The mass spectra in (b–d) are for the red, blue, and black extractions marked in (a), respectively; they were normalized such that the highest percentage of each color is assigned the same height.

ion gauge readings of 2×10^{-7} torr and 150 s exposures. The data in panels (c) and (d) are for 2×10^{-6} torr and 150 s exposures.

The black, blue, and red traces in panels (a) and (b) display the same trend of modest decay of X_{HDO} for a few tens of seconds after D_2O and H_2O are first admitted to the chamber followed by fairly constant values. The results were reproducible over a long period of time, and we attribute the random fluctuations to S/N. The traces in panels (a) and (b) were recorded on the same day. In panels (c) and (d), the red and blue traces were recorded on the same day, whereas the black trace was recorded a month earlier. No remarkable differences are seen. Larger HDO fractions than those shown in Figure 6 could be observed for different exposure histories. The HDO fractions shown are typical of our results for the stated pressure readings.

As shown in Figure 6, the degree of H/D scrambling depends on the chamber pressure during deposition: the higher the pressure reading, the smaller the degree of scrambling. Figure 7 shows an example of this trend with the chamber and array at 300 K, while other conditions were similar to those of Figure 6. The 300 K data display this effect more clearly because of their larger HDO percentages. Again, scrambling becomes less efficient as the pressure is raised. We attribute this to the availability of active sites. When the pressure is high a smaller fraction of the adsorbed molecules can be trapped at active sites and undergo H/D exchange.

Figures 6 and 7 show an order-of-magnitude difference between the HDO fractions obtained at 2×10^{-7} torr, namely, with versus without liquid nitrogen in the cooling tube. Examples of additional mass spectra are given in the Supporting Information. The difference can be explained in terms of the geometrical arrangement. Molecules in the main chamber have an opportunity to pass through its topmost opening (Figure 3), where cryopumping is efficient. A detailed explanation is given in Appendix 1. It is shown that the rate with which molecules pass from the main chamber into the upper region is several times larger than the pump rate of the turbomolecular pump. H/D exchange is particularly efficient in the upper region at 300 K. However, when the cooling tube contains liquid nitrogen, water molecules that enter this upper region are efficiently trapped there, and H/D scrambling is thwarted.

III.2. Pulsed Heating of the Nanoparticle Array. Films deposited on the cold array were exposed to pulsed 532 nm radiation: 10 ns, 0.4 mJ, ~0.5 mm diameter at the film. This radiation does not interact with H_2O, D_2O, N_2O_4, or the substrate due to their negligible 532 nm absorption cross sections. Some photoexcitation of free NO_2 takes place (~5%),[52,53] as discussed in Section II.

The gold nanoparticles absorb 532 nm radiation readily via one or more plasmon resonances and transitions that originate from gold d-bands. These excitations convert rapidly (picosecond time scale) to heat, and the maximum temperature achieved by isolated gold nanoparticles subjected to even modest radiation intensity can be high.[55] Though the crystal quartz substrate has good low-temperature thermal conductivity,[56] the rapid temperature rise of the nanoparticles compromises heat transfer from the array to the substrate. For example, such precipitous change in thermal conductivity versus temperature underlies the use of sapphire as a thermal

DOI: 10.1021/acs.jpca.7b04560
J. Phys. Chem. A 2017, 121, 4968–4981

switch.[57] Sapphire has high thermal conductivity at low temperature, but this changes to significantly lower thermal conductivity at high temperature. Estimating nanoparticle temperature is challenging, and it also presupposes that temperature can be usefully defined under highly nonequilibrium conditions over nanometer length scales. Thus, it is not clear a priori that temperature will prove to be an applicable metric for molecules undergoing ejection into vacuum under the present experimental conditions. Molecular-level modeling will be required to deal quantitatively with energy transfer to the substrate and to molecules being heated by the nanoparticles.

III.3. Heating Layers of D_2O + HDO and H_2O + HDO. Mass spectra were recorded with good S/N ratio following pulsed laser irradiation of the cold array covered with freshly deposited ASW films. As many as eight spots on a fresh film were irradiated by rastering the array, each with a single pulse, and the resulting temporal profiles of the ions monitored in the gaseous plume were summed to give profiles such as the one shown in Figure 8a. This profile consists of successive TOF spectra, each having duration of 10 μs. Expansion of the horizontal axis enables individual TOF spectra to be perused (not shown). Panels (b)−(d) show the corresponding mass spectra for the respective 10 μs "extractions" indicated with the red, blue, and black arrows in (a). The mass spectra do not differ significantly throughout the profile except for lower S/N at longer extraction times.

The mass spectra were converted to isotopologue fractions or percentages using the expressions derived in Appendix 2. Profiles and mass spectra such as those shown in Figure 8 were obtained in different sets of experiments. The results are summarized in Table 1, which gives the average values in the last row. Of course, the differences in isotopologue percentage are largest for HDO. These differences can be attributed in part to exposure history as described above. The enhanced H/D scrambling values obtained in the presence of NO_2/N_2O_4 (Section III.4) are judged against the values in Table 1.

Table 1. Isotopologue Percentages from 39 ML D_2O + HDO and 50 ML H_2O + HDO Films Desorbed by Pulsed Irradiation[a]

trial	% D_2O	% HDO	% H_2O
1	31.6	15.3	53.1
2	35.7	12.5	51.8
3	32.3	14.3	53.4
4	31.4	12.7	55.9
5	32.2	11.7	56.1
6	32.4	11.3	56.3
average	32.6	13.0	54.4

[a]532 nm, 10 ns, 0.4 mJ, 0.5 mm diameter.

The qualitative features seen in Figure 8 were reproduced in measurements performed under a broad range of conditions: film thickness, laser fluence, different extractions within a profile, and so on. Of course, HDO is always observed in mass spectra recorded following pulsed laser heating of the cold array coated with alternate layers of D_2O + HDO and H_2O + HDO. The fractions of HDO vary from as little as 0.11 to as much as 0.15. This modest range is attributable to exposure history, which influences H/D scrambling on 300 K surfaces. The observed HDO arises, in general, from two sources: the HDO that is present in the D_2O + HDO and H_2O + HDO layers, and the HDO that arises from photoinitiated H/D scrambling that takes place following irradiation of the gold nanoparticles. The latter is the approximate amount of H/D scrambling that would be observed in ejected water, if there were no HDO present in the deposited layers. We did not establish the percentage H/D scrambling that is due solely to photoinitiated heating of the gold nanoparticles, and in the Supporting Information we present cases that show how the relative contribution of these two sources of HDO might affect the results.

III.4. NO_2 Hydrolysis on ASW. An important feature of the present study is that each gold nanoparticle acts, to a considerable degree, as an independent source of material ejected into vacuum. This differs qualitatively from our earlier work with $D_2O/H_2O/N_2O_4$ films that were subjected to photoexcitation of an embedded N_2O_4 layer to create a heated stratum, as indicated in Figure 2c.[32] The transport mechanism there was passage of heated material from the embedded layer to vacuum via fissures that were created when thermal and pressure gradients fractured the ASW. Heated fluid entrained molecules from the transition region (i.e., the melting fissure walls) on its way to vacuum. We were also able to use NO_2 hydrolysis to create nitric acid. The presence of protons was inferred from the efficient H/D scrambling they bring about.

These experiments yielded interesting results but could not provide a direct comparison between H/D scrambling with versus without N_2O_4. In addition, theoretical modeling at the molecular level was not feasible, because the number of molecules that would have been required in the calculation was prohibitively large, and little was known about the fissures. The nanoscale heat sources used in the present study are amenable to molecular-level modeling, because one need only deal with a single nanoparticle and its immediate environment.

Dosing with NO_2 creates N_2O_4 efficiently, whenever coverage is sufficient to pair nearly all of the NO_2. In our previous study, buried N_2O_4 layers were created by dosing up to 60 L of NO_2, and in all cases pronounced H/D scrambling was observed.[32] In contrast, the NO_2 exposure used in the data shown in Figure 9 was modest: ∼1 L. Such small dosages of NO_2 have no meaning in terms of monolayers, and therefore we use Langmuirs to describe their deposition. The low NO_2 dosage is likely to result in a combination of NO_2 and N_2O_4 scattered sporadically about the ASW surface, with some embedding. Even this modest amount of N_2O_4/NO_2 dosed atop layers of D_2O and H_2O (including a small amount of background HDO, as described earlier) proved sufficient to bring about greatly enhanced scrambling, as shown in Figure 9. This demonstrates the creation of an acidic region near the surface.

Efficient H/D scrambling was found to take place over a broad range of conditions: different H_2O and D_2O thickness, NO_2 dosage, laser fluence, and location of the NO_2/N_2O_4. The result shown in Figure 9 is representative. Additional data are presented in the Supporting Information. Note that with NO_2 exposure of ∼1 L, the result shown in Figure 9 has 36.6% of the released water as HDO compared to 14.3% in its absence. The red and black bars are for different experiments, so no attempt was made to subtract the amount of HDO that is due to H/D scrambling on the 300 K surfaces. Nonetheless, on the basis of all of the data acquired to date, we are confident that it is a significant fraction of the HDO observed without NO_2. For example, if half of the HDO represented by the black bar arises from 300 K surfaces, and the same amount is assigned to the red bar, removing this background would reduce the HDO bars

DOI: 10.1021/acs.jpca.7b04560
J. Phys. Chem. A 2017, 121, 4968−4981

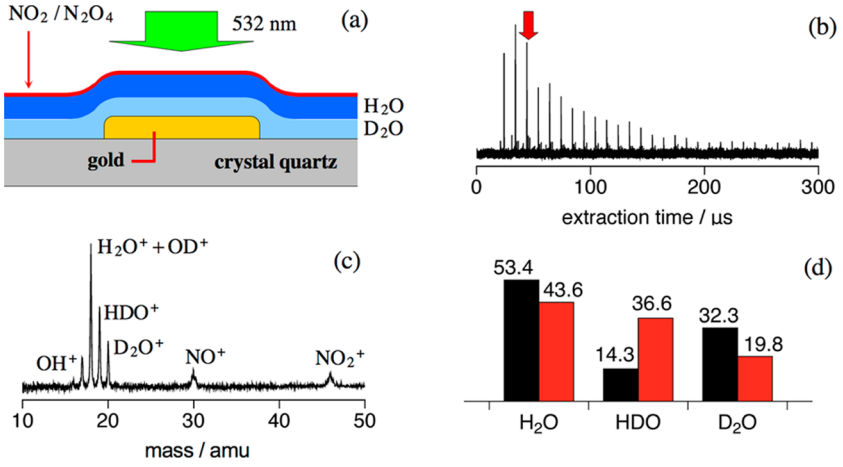

Figure 9. (a) 532 nm radiation excites gold nanoparticles, initiating transport to vacuum following deposition of ~1 L of NO_2 atop 39 ML of D_2O and 50 ML of H_2O. (b) The extraction labeled with a red arrow yielded the mass spectrum in (c), which shows significant scrambling. (d) The red bars are obtained from the mass spectrum in (c); the black bars are from Trial 3 in Table 1. If scrambling on 300 K surfaces is taken into account, the proton-enhanced scrambling is more pronounced than 36.6 vs 14.3 (see Supporting Information).

to 7.15% (black) and 29.45% (red). See the Supporting Information for a detailed analysis. Thus, there is no doubt that the observed enhancement in H/D scrambling via proton transfer (Grotthuss mechanism)[58] is significant.

Theoretical modeling by the Gerber and Finlayson-Pitts groups has provided a mechanism for the formation of HNO_3. They examined $ONONO_2(H_2O)_n$ clusters and predicted that the $ONONO_2$ isomer of N_2O_4 converts rapidly to the nitrosonium nitrate ion pair $NO^+NO_3^-$ in watery environments, yielding HONO and HNO_3. We find that, under conditions that facilitate accessing the $ONONO_2$ configuration, such as exist in our experiments, enough nitric acid is formed to bring about significant H/D scrambling. The time that material spends in transit to vacuum is most likely much less than the 10 ns laser pulse duration. For example, material that travels 20 nm at a speed of 20 m s^{-1} does so in 1 ns. Thus, proton-catalyzed H/D scrambling takes place efficiently and on a short time scale.

III.5. Is HNO_3 Produced on 300 K Surfaces and Deposited on ASW? Finally, it is necessary to establish whether HNO_3 is produced on 300 K surfaces and then desorbs and deposits on the low-temperature films. If this happens, protons will be forthcoming and accelerate H/D scrambling. This possibility was checked using TOFMS measurements analogous to those presented in Figure 5.

Figure 10 shows the mass spectrum obtained 2.5 cm above the array when H_2O and NO_2 were flowed simultaneously, with partial pressure readings of 1×10^{-5} and 2×10^{-5} torr, respectively, with all surfaces at 300 K. Summing 750 spectra yielded good S/N with no hint of HNO_3^+ at 63 amu. The 70 eV mass spectrum of HNO_3 has ion ratios of $[NO_2^+]/[NO^+] = 1.96$ and $[NO_2^+]/[HNO_3^+] = 45.5$.[59] We interpret the ratio 45.5 to be an upper bound, because the authors used a metal hypodermic needle to deliver HNO_3 to the ionization region of their mass spectrometer, and HNO_3 decomposes on metal surfaces.[59] Figure 10 shows that the NO_2^+ peak is larger than any HNO_3^+ peak that might be buried in the noise by a factor of at least 2×10^4.

This factor needs to be converted to an inequality that accounts for the relative 70 eV ionization cross sections of NO_2 and HNO_3 and their cracking patterns. The relevant expression is

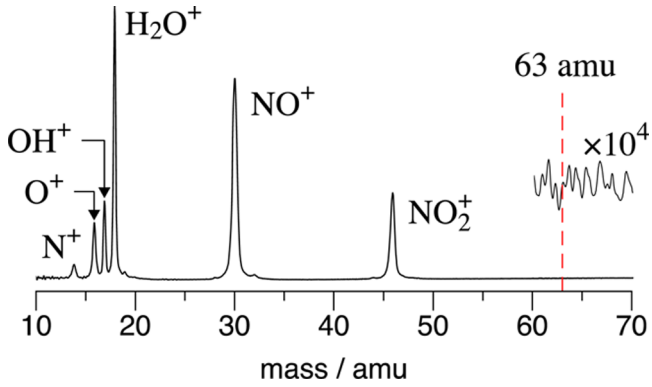

Figure 10. This spectrum was obtained with H_2O and NO_2 at pressure readings of 1×10^{-5} and 2×10^{-5} torr, respectively. Scale expansion (1×10^4 between 60 and 70 amu, 49-point smooth) shows no hint of an HNO_3^+ signal at 63 amu (dashed line). A sloping baseline in the 1×10^4 expansion region (imperceptible without scale expansion) was removed.

$$\frac{[NO_2]}{[HNO_3]} = \frac{\sigma_{ion}^{HNO_3}}{\sigma_{ion}^{NO_2}} \frac{S_{46^+}}{S_{63^+}} \frac{F_{63^+}^{HNO_3}}{F_{46^+}^{NO_2}} \quad (1)$$

where S_{46^+}/S_{63^+} is the ratio of signal amplitudes at 46 and 63 amu. The parameter $F_{46^+}^{NO_2}$ is the NO_2^+ fraction for the parent ion in 70 eV ionization, and likewise for $F_{63^+}^{HNO_3}$. Their values are 0.20 and 0.013, respectively.[59] The cross-section ratio $\sigma_{ion}^{HNO_3}/\sigma_{ion}^{NO_2}$ was taken to be 1.33. We could not find a literature value for $\sigma_{ion}^{HNO_3}$, so we assumed that the heavy atoms contribute equally to the 70 eV ionization cross section. Putting these numbers into eq 1 yields for our experiment (i.e., $S_{46^+}/S_{63^+} > 2 \times 10^4$) the limit:

$$\frac{[NO_2]}{[HNO_3]} > 1.7 \times 10^3 \quad (2)$$

Thus, little if any HNO_3 deposits on the films.

The case against HNO_3 deposition on the cold array is even stronger. On the one hand, in Section III.1.c and Appendix 1 we saw that active surface sites in the upper region that leads to the Fourier transform infrared (FTIR) tier account for most of the HDO that is detected above the array when the cooling

DOI: 10.1021/acs.jpca.7b04560
J. Phys. Chem. A 2017, 121, 4968−4981

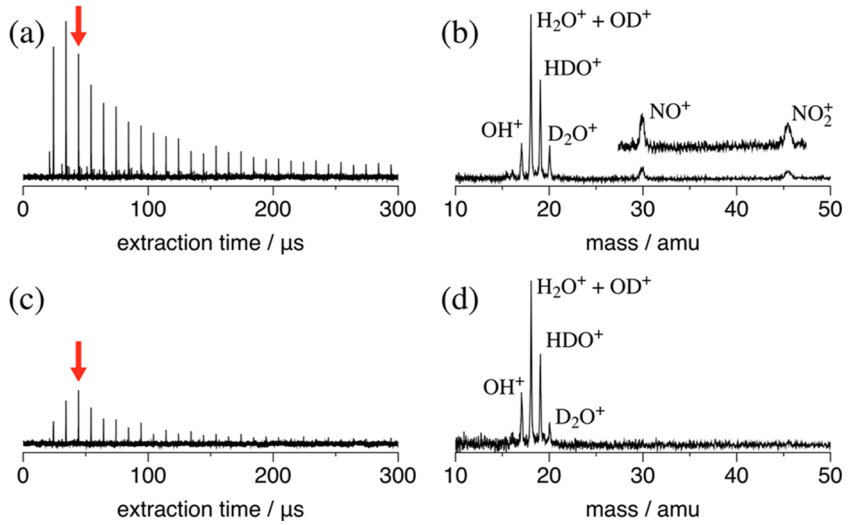

Figure 11. (a, b) First-pulse irradiation of eight spots on a fresh film (39 ML of D_2O, followed by 50 ML of H_2O, and then ~1 L of NO_2), each with a single laser pulse. The extractions used for the mass spectra are indicated with red arrows. (c, d) A second laser pulse incident on the same spots. Laser energy was 0.6 mJ.

tube is at 300 K. On the other hand, this HDO amount is reduced dramatically when the cooling tube is at 77 K. If the active sites in the upper region also catalyze the formation of HNO_3 at 300 K, this source of HNO_3 will be eliminated when the cooling tube is at 77 K.

On the basis of the data shown in Figure 10, the inequality in eq 2, and the analysis in Appendix 1, we conclude that NO_2/N_2O_4 hydrolysis yields nitric acid, and the resulting protons are responsible for the acceleration of H/D scrambling observed in our experiments.

III.6. Subsequent Pulses. To demonstrate the efficient heating enabled by the use of gold nanoparticles, Figure 11 compares data for first and second pulses. Signal from the second pulse is always much smaller than that from the first pulse. A third pulse sometimes yields acceptable S/N, but it is not possible to take reliable data. Notice that NO^+ and NO_2^+ features are absent with the second pulse. The relatively small signal for the second pulse is consistent with efficient removal of material from above the gold particles with the first pulse.

IV. SUMMARY AND CONCLUSIONS

We have devised and implemented a novel experimental strategy for studying fragile nanoscale samples in which dynamical processes are initiated using pulsed radiation: a marriage, so to speak, of nanoimprint lithography and pulsed laser photoinitiation. The present study focuses on ASW (H_2O and D_2O) and presents preliminary results in which H/D scrambling is accelerated greatly by protons when nitric acid is produced following rapid, thermally driven NO_2 hydrolysis. The method also enables theoretical modeling and simulations to be performed at the atomistic (molecular) level, as opposed to fluid mechanics or thermodynamics-based analyses.

Nanoimprint lithography is a finely honed technology that is ideal for preparing nanoparticle arrays that suit our purposes. The idea is to use a single laser pulse to heat an array comprising millions of nanoparticles upon which a doped or undoped ASW film has been deposited at low temperature under UHV conditions. The number of nanoparticles irradiated with a 0.5 mm diameter laser beam is roughly 10^6, resulting in signal averaging and good single-pulse S/N. The nanoparticles are spaced sufficiently far from one another to ensure that each acts independently, in which case the recorded signal is the sum of signals from roughly 10^6 "nanoexperiments".

In the case of thin films of ASW deposited on the array of nanoparticles, the application of a single laser pulse alters the irradiated area dramatically and irreversibly. This places a stringent requirement on data acquisition. Namely, good S/N must be achieved when irradiating a given area with a single pulse. It can be informative to apply second, third, etc. pulses to the same area that was irradiated by the first pulse. Again, the pulses are isolated: the second pulse results are summed with each other; the third pulse results are summed with each other; and so on. The sample can be rastered to enable different regions of the array to be used with a series of laser pulses, but again, only results from a given pulse (first, second, third, etc.) are summed.

In this first report, we demonstrate principles and illustrate key aspects of this novel approach, including subtle and nuanced details. Films were grown when D_2O and H_2O were introduced to the chamber sequentially through separate inlets. The data presented herein are for deposition of a D_2O layer followed by deposition of an H_2O layer, in each case with some HDO contaminant. Reversing the order of the depositions, that is, H_2O followed by D_2O, resulted in no surprises.

Deposition of H_2O and D_2O introduces HDO through H/D scrambling on the 300 K surfaces. While this can be exasperating, we showed how to minimize this HDO background through exploitation of the fact that deposition at higher pressure lessens the fractional participation of surface sites that are responsible for H/D scrambling. In other words, when all of the surface active sites are occupied, increasing the number of molecules incident on the surface does not yield more HDO. In addition, we show how H/D scrambling on 300 K surfaces can be taken into account through an estimate based on mass spectra of gas-phase molecules recorded above the cold array during deposition.

The experiments were taken a step further to illustrate the viability of the method in more complex situations, such as those involving chemical transformations. A modest amount of NO_2 was deposited on the ASW film, and the array was irradiated. This resulted in the production of nitric acid, and the

DOI: 10.1021/acs.jpca.7b04560
J. Phys. Chem. A 2017, 121, 4968−4981

resulting protons catalyzed H/D scrambling. Indeed, enhancement of H/D scrambling was observed over a broad range of conditions. We also showed that HNO_3 is not, to any measurable extent, deposited on the 100 K sample, that is, having been created on exposed 300 K surfaces followed by desorption and deposition on the cold array. As mentioned earlier, theoretical studies[43−46] predict that, if the $ONONO_2$ configuration is reached in a watery environment, the nitrosonium nitrate ion pair $NO^+NO_3^-$ will follow in just 20−30 fs,[43] and HONO and HNO_3 will follow shortly thereafter.[45] The present experimental conditions were conducive to sampling the $ONONO_2$ configuration, and the results presented herein are consistent with the proposed mechanism, though not proof of its sole participation. The rapid H/D scrambling observed in these experiments invites atomistic modeling and simulations of a single nanoparticle and its evolving environment. It can also be used to study the emergence of acidity in other systems.

The combination of nanoimprint lithography and photoexcitation presents many opportunities for future research. It is straightforward, in the hands of experts, to prepare arrays of discs, rectangles, rods, pillars, cones, and more exotic shapes. Such shapes enable one to design conduits through which heated material passes to vacuum, for example, azimuthally symmetric chimneys (using disks), fissures (using rods), and so on. Successive deposition-photoejection cycles, combined with directed dosing, enables the construction of "chimneys" that extend from the particle to vacuum through films of variable thickness and composition.

The method should enable, for example, studies of transport through fissures, which are relevant to the moons Enceladus and Europa. Analogous phenomena can be examined in the nanoscale microcosms, albeit on vastly different scales. For example, embedded layers of $^{12}CO_2$ and $^{13}CO_2$ of varying thickness and location can be used to examine the entrainment of material that is stripped from melting walls by watery fluid on its way to vacuum. Such studies, in concert with atomistic modeling and simulation, will further our understanding of what might transpire in the passage of water through fissures. A significant amount of CO_2 is present in the effluent that issues from the fissures on Enceladus; a considerable fraction of it might be entrained from the melting walls through the passage of water to the moon's surface. This raises intriguing issues such as aggregation of CO_2 in pockets and its explosive release accompanied by water.[28] Recent reports on observations from the Cassini mission and the Hubble telescope on ice eruptions on Enceladus and Europa underscore the continued keen interest in these phenomena.[14,60]

APPENDIX 1. MINIMIZING SURFACE-CATALYZED HDO PRODUCTION

There is an order-of-magnitude difference between the HDO fractions obtained at 2×10^{-7} torr with versus without liquid nitrogen in the cooling tube, respectively, Figures 6 and 7. This surprised us at first. We show here that it can be explained through consideration of the geometrical arrangement. A significant fraction of the molecules in the main chamber pass through its topmost opening, which accommodates the cooling tube and leads to the FTIR tier. This affects the deposition of HDO onto the cold array, as discussed below.

Figure 3 indicates this region in relation to the main chamber, and Figure A1.1 elaborates its features. The topmost flange is connected to a UHV gate valve (not shown), which is

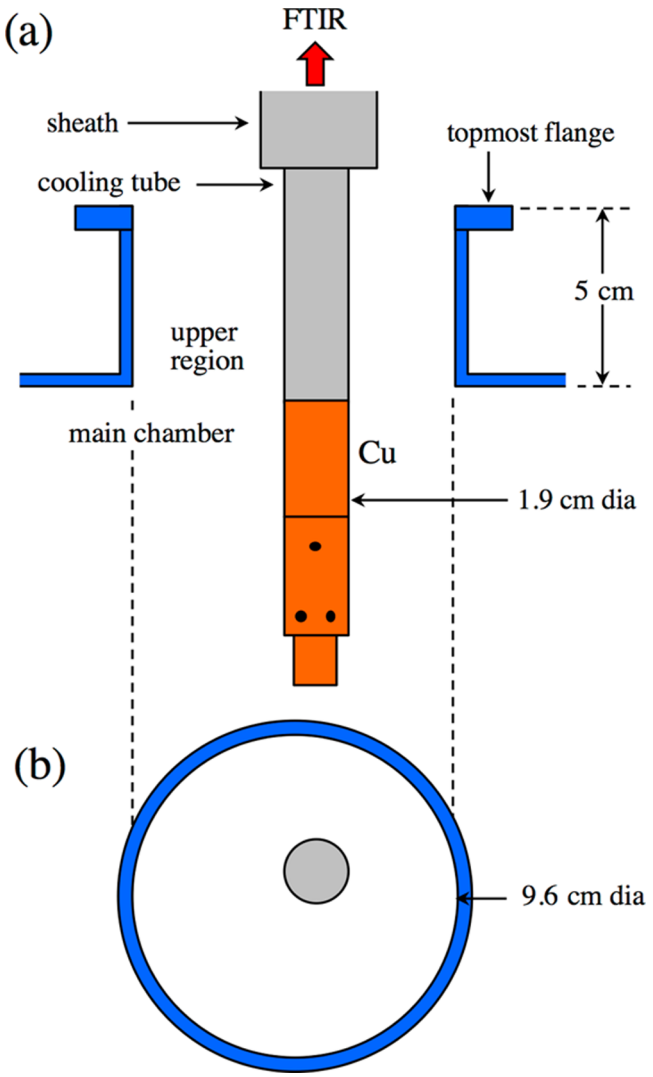

Figure A1.1. Expanded and elaborated view of the uppermost part of the main chamber shown in Figure 3. (a) Molecules that enter the upper region without liquid nitrogen in the cooling tube explore different surfaces and have opportunities to undergo H/D scrambling. When the cooling tube contains liquid nitrogen the situation differs qualitatively. A large amount of water is trapped on the cooling tube and does not reenter the main chamber. (b) This cross-sectional view depicts the cooling tube (gray), which is offset from the center to facilitate deposition. Molecules that miss the cooling tube can be adsorbed on the blue wall and reemitted. This cycle results in efficient trapping of water molecules that enter the upper region.

connected to the FTIR tier. The rate with which molecules pass from the main chamber into the upper region is roughly 4.4 times larger than the pump rate of the 600 L/s turbomolecular pump, despite the smaller opening of the former. The volumetric flow rate into the upper region is estimated by multiplying its cross-sectional area (72 cm^2) times 3.67×10^4 cm/s (i.e., $v_z = (kT/m)^{1/2}$), yielding 2640 L/s.

The net flux of water molecules into the upper region is zero with everything at 300 K. There will be H/D scrambling, but in steady state the number of water molecules that enter the upper region is equal to the number of water molecules that leave it.

Water molecules in the 300 K upper region can engage in adsorption, physisorption, chemisorption, H/D scrambling, desorption, elastic scattering, inelastic scattering, etc. Local transport on a surface following adsorption, including capture

DOI: 10.1021/acs.jpca.7b04560
J. Phys. Chem. A 2017, 121, 4968−4981

at active sites and H/D scrambling, takes place in competition with desorption. A desorbed molecule passes through vacuum and can be adsorbed when it contacts another surface. The upper region, with its stainless steel coldfinger and sheath, gate valve, stainless steel FTIR tier, and other exposed parts is more conducive to H/D scrambling than the electropolished main chamber. When the cooling tube is at 300 K, H/D scrambling in the upper region plays an important role, because a large fraction of the admitted molecules spend time in the upper region.

Referring to Figure A1.1a, the situation changes when the cooling tube is at 77 K, enabling it to trap molecules that enter the upper region. Cold parts in the main chamber also trap molecules, but the upper region accounts for most of the trapping because of its large aperture.

Thermal desorption takes place most frequently with an angular distribution close to cos θ, where θ is relative to the surface normal.[61,62] When the cooling tube is at 77 K, part of the desorption lobe is intercepted by it, and these molecules are trapped. Molecules that miss the cooling tube encounter the wall, where they can adsorb. Their subsequent desorption again results in some of them being trapped. This cycle continues, until a given molecule either passes from the upper region into the main chamber or is trapped. Thus, a modest amount of HDO enters the main chamber from the upper region when the cooling tube is at 77 K, whereas a relatively large amount of HDO enters the main chamber when it is at 300 K.

This model is consistent with the dramatic effect on H/D scrambling when the array was cold versus 300 K. Such trapping also plays a role in the NO_2 hydrolysis experiments discussed in Section III.4. It also underscores the fact that subtle differences between configurations can yield different results in experiments of this nature.

APPENDIX 2. CONVERTING MASS SPECTRA TO PERCENTAGES OF H_2O, D_2O, AND HDO

To convert mass spectra obtained from deposits of H_2O, D_2O, and HDO to concentration ratios, parent ion cracking patterns (for electron impact ionization at 70 eV) need to be taken into account. This has been done using the procedure that follows. The measured areas of the mass peaks at 20, 19, and 18 amu, denoted A_{20}, A_{19}, and A_{18}, respectively, are proportional to ion concentrations (denoted by brackets). Because the proportionality constants are equal for the different A_{ij} values, we can use

$$A_{20} = [D_2O^+] \tag{A.1}$$

$$A_{19} = [HDO^+] \tag{A.2}$$

$$A_{18} = [H_2O^+] + [OD^+]_{D_2O^+} + [OD^+]_{HDO^+} \tag{A.3}$$

where $[OD^+]_{D_2O^+}$ is the OD^+ concentration from $[D_2O^+]$ fragmentation, while $[OD^+]_{HDO^+}$ is from $[HDO^+]$ fragmentation. Parent ions yield daughter ions according to

$$[OD^+]_{D_2O^+} = 0.27[D_2O^+] \tag{A.4}$$

$$[OD^+]_{HDO^+} = 0.7 \times 0.27[HDO^+] \tag{A.5}$$

$$[OH^+]_{H_2O^+} = 0.27[H_2O^+] \tag{A.6}$$

$$[OH^+]_{HDO^+} = 0.3 \times 0.27[HDO^+] \tag{A.7}$$

Some O^+ is produced, though not enough to warrant its inclusion. The multiplier 0.27 was obtained from the ratio observed in our TOFMS using pure H_2O and D_2O samples. The multipliers 0.7 and 0.3 are from ref 63, which reports that OD^+ is favored over OH^+ by a factor of 2.1.

Adding eqs A.1–A.3 and defining $A_T \equiv A_{18} + A_{19} + A_{20}$, where T stands for total, yields

$$A_T = [D_2O^+] + [HDO^+] + [H_2O^+] + [OD^+]_{D_2O^+} + [OD^+]_{HDO^+} \tag{A.8}$$

$$= A_{20} + A_{19} + [H_2O^+] + 0.27A_{20} + (0.7)(0.27)A_{19} \tag{A.9}$$

which rearranges to give the fraction of $[H_2O^+]$. Including eqs A.1 and A.2 gives

$$\frac{[H_2O^+]}{A_T} = 1 - 1.27\frac{A_{20}}{A_T} - 1.19\frac{A_{19}}{A_T} \tag{A.10}$$

$$\frac{[D_2O^+]}{A_T} = \frac{A_{20}}{A_T} \tag{A.11}$$

$$\frac{[HDO^+]}{A_T} = \frac{A_{19}}{A_T} \tag{A.12}$$

The concentrations of neutral H_2O, D_2O, and HDO are proportional to H_2O^+, D_2O^+, and HDO^+, respectively, because these yield OH^+, OD^+, and (OH^+ + OD^+) respectively, with a ratio of 0.27, for example, $[OH^+]/[H_2O^+] = 0.27$. Thus, the measured areas A_{20}, A_{19}, and A_{18} yield the neutral fractions:

$$F_{D_2O} = \frac{A_{20}}{A_T} \tag{A.13}$$

$$F_{HDO} = \frac{A_{19}}{A_T} \tag{A.14}$$

$$F_{H_2O} = 1 - 1.27\frac{A_{20}}{A_T} - 1.19\frac{A_{19}}{A_T} \tag{A.15}$$

These fractions, multiplied by 100, give the percent populations listed in Table 1 and Figure 9, which describe results on H/D scrambling observed following pulsed irradiation.

When examining trends in H/D scrambling in experiments such as those described in Section III.1 and Figures 6 and 7, the HDO fraction is small. Therefore, approximate ratios based on peak areas A_{20}, A_{19}, and A_{18} are sufficient, as mentioned in the main text. Here we shall compare the ratios $A_{19}/(A_{20} + A_{19})$ and $A_{19}/(A_{18} + A_{19})$ to their counterparts $[HDO]/[D_2O + HDO]$ and $[HDO]/[H_2O + HDO]$, respectively. Starting with the first ratio

$$\frac{A_{19}}{A_{20} + A_{19}} = \frac{F_{HDO}}{F_{D_2O} + F_{HDO}} = \frac{[HDO]}{[D_2O + HDO]} \tag{A.16}$$

we see that no approximation is involved. The ratio of peak areas gives the ratio of concentrations of the corresponding neutrals. This was referred to in the text as X_{HDO}, where it was applied to the case of only D_2O admitted to the chamber, in which case $A_{18} = 0$. Even if H_2O were also admitted, the above relationship would not change, because it depends only on the 19 and 20 amu signals. That is, there is no additional contribution to these signals from the presence of H_2O; they

DOI: 10.1021/acs.jpca.7b04560
J. Phys. Chem. A 2017, 121, 4968–4981

are due solely to HDO and D_2O, respectively. The situation is different for $A_{19}/(A_{18} + A_{19})$. To see how this relates to $[HDO]/[H_2O + HDO]$, write

$$\frac{[HDO]}{[H_2O + HDO]} = \frac{F_{HDO}}{F_{H_2O} + F_{HDO}} = \frac{A_{19}}{A_T - 1.27A_{20} - 1.19A_{19} + A_{19}} \quad (A.17)$$

When only H_2O is admitted to the chamber, $A_{20} = 0$, and this becomes

$$\frac{[HDO]}{[H_2O + HDO]} = \frac{A_{19}}{A_{18} + A_{19} - 0.19A_{19}} \quad (A.18)$$

Now use the fact that the peak at 19 amu is relatively small:

$$\frac{[HDO]}{[H_2O + HDO]} = \frac{A_{19}}{A_{18} + A_{19}} \frac{1}{1 - \frac{0.19A_{19}}{A_{18} + A_{19}}} \approx \frac{A_{19}}{A_{18} + A_{19}}\left(1 + \frac{0.19A_{19}}{A_{18} + A_{19}}\right) \quad (A.19)$$

For $A_{19}/A_{18} = 0.1$, the second term in the parentheses has a value of 0.017, which is a minor correction to data such as those in Figures 6 and 7. Thus, peak areas can often be used.

■ ASSOCIATED CONTENT

Supporting Information

The Supporting Information is available free of charge on the ACS Publications website at DOI: 10.1021/acs.jpca.7b04560.

Effect of cooling the array on H/D scrambling, mass spectra, effect of varying the percentage of HDO in the deposited layers, varying the NO_2 layer thickness, varying the NO_2 location in the film (PDF)

■ AUTHOR INFORMATION

Corresponding Authors

*E-mail: reisler@usc.edu. (H.R.)
*E-mail: wittig@usc.edu. (C.W.)

Author Contributions

The manuscript was written through contributions of all authors. All authors have given approval to the final version of the manuscript.

Notes

The authors declare no competing financial interest.

■ ACKNOWLEDGMENTS

Y.L. acknowledges financial support from the Northrop Grumman Institute of Optical Nanomaterials and Nanophotonics (NG-ION2). H.R. acknowledges support from an endowed chair, Lloyd Armstrong Jr. Chair in Science and Engineering, and from the National Science Foundation Grant No. CHE-1265725. C.W. acknowledges financial support from an endowed chair: Paul A. Miller Professor of Letters, Arts, and Sciences, and from USC College Research Support Account No. 2218151093.

■ REFERENCES

(1) Angell, C. A. Amorphous Water. *Annu. Rev. Phys. Chem.* **2004**, *55*, 559−583.
(2) Jenniskens, P.; Blake, D. F. Structural Transitions in Amorphous Water Ice and Astrophysical Implications. *Science* **1994**, *265*, 753−756.
(3) Smoluchowski, R. Amorphous Ice on Saturnian Rings and on Icy Satellites − Its Formation, Stability, and Observability. *Science* **1978**, *201*, 809−811.
(4) Leger, A.; Klein, J.; Cheveigne, S. D.; Guinet, C.; Defourneau, D.; Belin, M. The 3.1 Micron Absorption in Molecular Clouds is Probably Due to Amorphous H_2O Ice. *Astron. Astrophys.* **1979**, *79*, 256−259.
(5) Whittet, D. C. B.; Bode, M. F.; Longmore, A. J.; Baines, D. W. T.; Evans, A. Interstellar Ice Grains in the Taurus Molecular Clouds. *Nature* **1983**, *303*, 218−221.
(6) Hama, T.; Watanabe, N. Surface Processes on Interstellar Amorphous Solid Water: Adsorption, Diffusion, Tunneling Reactions, and Nuclear-Spin Conversion. *Chem. Rev.* **2013**, *113*, 8783−8839.
(7) Allamandola, L. J.; Bernstein, M. P.; Sandford, S. A.; Walker, R. L. Evolution of Interstellar Ices. *Space Sci. Rev.* **1999**, *90*, 219−232.
(8) Tielens, A. G. G. M. The Molecular Universe. *Rev. Mod. Phys.* **2013**, *85*, 1021−1081.
(9) Savin, D. W.; Brickhouse, N. S.; Cowan, J. J.; Drake, R. P.; Federman, S. R.; Ferland, G. J.; Frank, A.; Gudipati, M. S.; Haxton, W. C.; Herbst, E.; Profumo, S.; Salama, F.; Ziurys, L. M.; Zweibel, E. G. The Impact of Recent Advances in Laboratory Astrophysics on Our Understanding of the Cosmos. *Rep. Prog. Phys.* **2012**, *75*, 036901.
(10) Ehrenfreund, P.; Charnley, S. B. Organic Molecules in the Interstellar Medium, Comets, and Meteorites: A Voyage from Dark Clouds to the Early Earth. *Annu. Rev. Astron. Astrophys.* **2000**, *38*, 427−483.
(11) Accolla, M.; Congiu, E.; Dulieu, F.; Manicò, G.; Chaabouni, H.; Matar, E.; Mokrane, H.; Lemaire, J. L.; Pirronello, V. Changes in the Morphology of Interstellar Ice Analogues after Hydrogen Atom Exposure. *Phys. Chem. Chem. Phys.* **2011**, *13*, 8037−8045.
(12) Vance, S.; Bouffard, M.; Choukroun, M.; Sotin, C. Ganymede's Internal Structure Including Thermodynamics of Magnesium Sulfate in Contact with Ice. *Planet. Space Sci.* **2014**, *96*, 62−70.
(13) Sparks, W. B.; Schmidt, B. E.; McGrath, M. A.; Hand, K. P.; Spencer, J. R.; Cracraft, M.; Deustua, S. E. Active Cryovolcanism on Europa. *Astrophys. J., Lett.* **2017**, *839*, L18.
(14) Waite, J. H.; Glein, C. R.; Perryman, R. S.; Teolis, B. D.; Magee, B. A.; Miller, G.; Grimes, J.; Perry, M. E.; Miller, K. E.; Bouquet, A.; et al. Cassini Finds Molecular Hydrogen in the Enceladus Plume: Evidence for Hydrothermal Processes. *Science* **2017**, *356*, 155−159.
(15) Glein, C.; Baross, J. A.; Waite, J. H., Jr. The pH of Enceladus' Ocean. *Geochim. Cosmochim. Acta* **2015**, *162*, 202−219.
(16) Porco, C.; DiNino, D.; Nimmo, F. How the Geysers, Tidal Stresses, and Thermal Emission Across the South Polar Terrain of Enceladus are Related. *Astron. J.* **2014**, *148*, 45.
(17) Nimmo, F.; Porco, C.; Mitchell, C. Tidally Modulated Eruptions on Enceladus: Cassini ISS Observations and Models. *Astron. J.* **2014**, *148*, 46.
(18) Hedman, M. M.; Gosmeyer, C. M.; Nicholson, P. D.; Sotin, C.; Brown, R. H.; Clark, R. N.; Baines, K. H.; Buratti, B. J.; Showalter, M. R. An Observed Correlation Between Plume Activity and Tidal Stresses on Enceladus. *Nature* **2013**, *500*, 182−184.
(19) Hurford, T. A.; Helfenstein, P.; Hoppa, G. V.; Greenberg, R.; Bills, B. G. Eruptions Arising from Tidally Controlled Periodic Openings of Rifts on Enceladus. *Nature* **2007**, *447*, 292−294.
(20) Hansen, C. J. Enceladus' Water Vapor Plume. *Science* **2006**, *311*, 1422−1425.
(21) Porco, C. C. Cassini Observes the Active South Pole of Enceladus. *Science* **2006**, *311*, 1393−1401.
(22) Hansen, C. J.; Esposito, L. W.; Stewart, A. I. F.; Meinke, B.; Wallis, B.; Colwell, J. E.; Hendrix, A. R.; Larsen, K.; Pryor, W.; Tian, F. Water Vapor Jets Inside the Plume of Gas Leaving Enceladus. *Nature* **2008**, *456*, 477−479.
(23) Waite, J. H., Jr.; Lewis, W. S.; Magee, B. A.; Lunine, J. I.; McKinnon, W. B.; Glein, C. R.; Mousis, O.; Young, D. T.; Brockwell, T.; Westlake, J.; Nguyen, M.-J.; Teolis, B. D.; Niemann, H. B.; McNutt, R. L., Jr.; Perry, M.; Ip, W.-H. Liquid Water on Enceladus

DOI: 10.1021/acs.jpca.7b04560
J. Phys. Chem. A 2017, 121, 4968−4981

from Observations of Ammonia and ^{40}Ar in the Plume. *Nature* **2009**, *460*, 487−490.
(24) Hansen, C. J.; Shemansky, D. E.; Esposito, L. W.; Stewart, A. I. F.; Lewis, B. R.; Colwell, J. E.; Hendrix, A. R.; West, R. A.; Waite, J. H., Jr.; Teolis, B.; Magee, B. A. The Composition and Structure of the Enceladus Plume. *Geophys. Res. Lett.* **2011**, *38*, L11202.
(25) May, R. A.; Smith, R. S.; Kay, B. D. The Molecular Volcano Revisited: Determination of Crack Propagation and Distribution During the Crystallization of Nanoscale Amorphous Solid Water Films. *J. Phys. Chem. Lett.* **2012**, *3*, 327−331.
(26) May, R. A.; Smith, R. S.; Kay, B. D. The Release of Trapped Gases from Amorphous Solid Water Films. I. ″Top-down″ Crystallization-induced Crack Propagation Probed Using the Molecular Volcano. *J. Chem. Phys.* **2013**, *138*, 104501.
(27) Smith, R. S.; Petrik, N. G.; Kimmel, G. A.; Kay, B. D. Thermal and Nonthermal Physiochemical Processes in Nanoscale Films of Amorphous Solid Water. *Acc. Chem. Res.* **2012**, *45*, 33−42.
(28) Rebolledo-Mayoral, O.; Stomberg, J.; McKean, S.; Reisler, H.; Wittig, C. Amorphous Solid Water (ASW): Pulsed Laser Ablation of ASW/CO_2 Thin Films. *J. Phys. Chem. C* **2012**, *116*, 563−569.
(29) Johari, G. P.; Hallbrucker, A.; Mayer, E. The Glass-Liquid Transition of Hyperquenched Water. *Nature* **1987**, *330*, 552−553.
(30) Johari, G. P.; Andersson, O. Vibrational and Relaxational Properties of Crystalline and Amorphous Ices. *Thermochim. Acta* **2007**, *461*, 14−43.
(31) Capaccioli, S.; Ngai, K. L. Resolving the Controversy on the Glass Transition Temperature of Water. *J. Chem. Phys.* **2011**, *135*, 104504.
(32) Stomberg, J.; McKean, S.; Larson, C.; Reisler, H.; Wittig, C. Amorphous Solid Water: Pulsed Heating of Buried N_2O_4. *J. Phys. Chem. C* **2015**, *119*, 14548−14560.
(33) Shekhar, A.; Nomura, K.-i; Kalia, R. K.; Nakano, A.; Vashishta, P. Nanobubble Collapse on a Silica Surface in Water: Billion-Atom Reactive Molecular Dynamics Simulations. *Phys. Rev. Lett.* **2013**, *111*, 184503.
(34) Shekhar, A.; Kalia, R. K.; Nakano, A.; Vashishta, P.; Alm, C. K.; Malthe-Sørenssen, A. Universal Stretched Exponential Relaxation in Nanoconfined Water. *Appl. Phys. Lett.* **2014**, *105*, 161907.
(35) Finlayson-Pitts, B. J; Pitts, J. N., Jr. *Chemistry of the Upper and Lower Atmosphere—Theory, Experiments, and Applications;* Academic Press: San Diego, CA, 2000.
(36) Elshorbany, Y.; Barnes, I.; Becker, K. H.; Kleffmann, J.; Wiesen, P. Sources and Cycling of Tropospheric Hydroxyl Radicals − An Overview. *Z. Phys. Chem.* **2010**, *224*, 967−987.
(37) Ramazan, K. A.; Syomin, D.; Finlayson-Pitts, B. J. The Photochemical Production of HONO During the Heterogeneous Hydrolysis of NO_2. *Phys. Chem. Chem. Phys.* **2004**, *6*, 3836−3843.
(38) Platt, U.; Perner, D.; Harris, G. W.; Winer, A. M.; Pitts, J. N. Observations of Nitrous Acid in an Urban Atmosphere by Differential Optical Absorption. *Nature* **1980**, *285*, 312−314.
(39) Winer, A. M.; Biermann, H. W. Long Pathlength Differential Optical Absorption Spectroscopy (DOAS) Measurements of Gaseous HONO, NO_2, and HCNO in the California South Coast Air Basin. *Res. Chem. Intermed.* **1994**, *20*, 423−445.
(40) Lammel, G.; Cape, J. N. Nitrous Acid and Nitrite in the Atmosphere. *Chem. Soc. Rev.* **1996**, *25*, 361−369.
(41) Harrison, R. M.; Peak, J. D.; Collins, G. M. Tropospheric Cycle of Nitrous Acid. *J. Geophys. Res.* **1996**, *101*, 14429−14439.
(42) Finlayson-Pitts, B. J.; Wingen, L. M.; Sumner, A. L.; Syomin, D.; Ramazan, K. A. The Heterogeneous Hydrolysis of NO_2 in Laboratory Systems and in Outdoor and Indoor Atmospheres: An Integrated Mechanism. *Phys. Chem. Chem. Phys.* **2003**, *5*, 223−242.
(43) Miller, Y.; Finlayson-Pitts, B. J.; Gerber, R. B. Ionization of N_2O_4 in Contact with Water: Mechanism, Time Scales, and Atmospheric Implications. *J. Am. Chem. Soc.* **2009**, *131*, 12180−12185.
(44) Lignell, H.; Varner, M. E.; Finlayson-Pitts, B. J.; Benny Gerber, R. Isomerization and Ionization of N_2O_4 on Model Ice and Silica Surfaces. *Chem. Phys.* **2012**, *405*, 52−59.
(45) Varner, M. E.; Finlayson-Pitts, B. J.; Benny Gerber, R. Reaction of a Charge-separated $ONONO_2$ Species with Water in the Formation of HONO: An MP2Molecular Dynamics Study. *Phys. Chem. Chem. Phys.* **2014**, *16*, 4483−4487.
(46) Gerber, R. B.; Varner, M. E.; Hammerich, A. D.; Riikonen, S.; Murdachaew, G.; Shemesh, D.; Finlayson-Pitts, B. J. Computational Studies of Atmospherically-relevant Chemical Reactions in Water Clusters and on Liquid Water and Ice Surfaces. *Acc. Chem. Res.* **2015**, *48*, 399−406.
(47) Pimentel, A. S.; Lima, F. C. A.; da Silva, A. B. F. The Isomerization of Dinitrogen Tetroxide: $O_2N-NO_2 \rightarrow ONO-NO_2$. *J. Phys. Chem. A* **2007**, *111*, 2913−2920.
(48) Pimentel, A. S.; Lima, F. C. A.; da Silva, A. B. F. The Asymmetric Dimerization of Nitrogen Dioxide. *Chem. Phys. Lett.* **2007**, *436*, 47−50.
(49) de Jesus Medeiros, D.; Pimentel, A. S. New Insights in the Atmospheric HONO Formation: New Pathways for N_2O_4 Isomerization and NO_2 Dimerization in the Presence of Water. *J. Phys. Chem. A* **2011**, *115*, 6357−6365.
(50) Liu, W.-G.; Goddard, W. A., III First-principles Study of the Role of Interconversion Between NO_2, N_2O_4, *cis*-ONO-NO2, and *trans*-ONO-NO2 in Chemical Processes. *J. Am. Chem. Soc.* **2012**, *134*, 12970−12978.
(51) Luo, G.; Chen, X. Ground-state Intermolecular Proton Transfer of N_2O_4 and H_2O: An Important Source of Atmospheric Hydroxyl Radical? *J. Phys. Chem. Lett.* **2012**, *3*, 1147−1153.
(52) Schneider, W.; Moortgat, G. K.; Tyndall, G. S.; Burrows, J. P. Absorption Cross-Sections of NO_2 in the UV and Visible Region (200 − 700 nm) at 298 K. *J. Photochem. Photobiol., A* **1987**, *40*, 195−217.
(53) Harder, J. W.; Brault, J. W.; Johnston, P. V.; Mount, G. H. Temperature Dependent NO_2 Cross Sections at High Spectral Resolution. *J. Geophys. Res. - Atmos.* **1997**, *102*, 3861−3879.
(54) Hawkins, S.; Kumi, G.; Malyk, S.; Reisler, H.; Wittig, C. Temperature Programmed Desorption and Infrared Spectroscopic Studies of Thin Water Films on MgO(100). *Chem. Phys. Lett.* **2005**, *404*, 19−24.
(55) Nedyalkov, N. N.; Imamova, S. E.; Atanasov, P. A.; Toshkova, R. A.; Gardeva, E. G.; Yossifova, L. S.; Alexandrov, M. T.; Obara, M. Interaction of Gold Nanoparticles with Nanosecond Laser Pulses: Nanoparticle Heating. *Appl. Surf. Sci.* **2011**, *257*, 5456−5459.
(56) de Haas, W. J.; Biermasz, T. The Thermal Conductivity of Quartz at Low Temperatures. *Physica* **1935**, *2*, 673−682.
(57) Sheikh, I. I.; Townsend, P. D. A Low Temperature Thermal Switch. *J. Phys. E: Sci. Instrum.* **1973**, *6*, 1170−1170.
(58) de Grotthuss, C. J. T. Sur La Décomposition De L'eau Et Des Corps Qu'elle Tient En Dissolution À L'aide De L'électricité Galvanique. *Ann. Chim.* **1806**, *58*, 54−73.
(59) O'Connor, C. S. S.; Jones, N. C.; Price, S. D. Electron-impact Ionization of Nitric Acid. *Int. J. Mass Spectrom. Ion Processes* **1997**, *163*, 131−139.
(60) Sparks, W. B.; Schmidt, B. E.; McGrath, M. A.; Hand, K. P.; Spencer, J. R.; Cracraft, M.; Deustua, S. E. Active Cryovolcanism on Europa? *Astrophys. J., Lett.* **2017**, *839*, L18.
(61) Wenaas, E. P. Equilibrium Cosine Law and Scattering Symmetry at the Gas−Surface Interface. *J. Chem. Phys.* **1971**, *54*, 376−388.
(62) Goodman, F. O.; Wachman, H. Y. *Dynamics of Gas-Surface Interactions;* Academic Press: New York, 1976.
(63) Furuya, K.; Koba, F.; Ogawa, T. Branching Ratio for the Production of OD(a) and OH(a) by Controlled Electron Impact on HOD. *J. Chem. Phys.* **1997**, *106*, 1764−1768.

DOI: 10.1021/acs.jpca.7b04560
J. Phys. Chem. A 2017, 121, 4968−4981